energies

MDPI

Article

Novel Three-Port Bidirectional DC/DC Converter with Three-Winding Coupled Inductor for Photovoltaic System

Yu-En Wu * and Kai-Cheng Hsu

Department of Electronic Engineering, National Kaohsiung University of Science and Technology, Kaohsiung 824, Taiwan; u0252009@nkfust.edu.tw

* Correspondence: yew@nkust.edu.tw; Tel.: +886-7-6011000 (ext. 32511)

Received: 19 January 2020; Accepted: 1 March 2020; Published: 3 March 2020

Abstract: This study proposes a novel three-port bidirectional converter with a three-winding coupled inductor and applies it to a photovoltaic (PV) system to step up the PV system output to a dc bus or dc load while charging the battery. When the PV output is insufficient, battery voltage is stepped up to the dc bus voltage, and when the dc bus has excess energy, it is stepped down to charge the battery. Thus, a three-port bidirectional high step-up/step-down converter is achieved. A three-winding common core coupled inductor is designed and implemented in the converter, and a full-wave doubler circuit is used on the high-voltage side to achieve a high step-up effect. Power switches and diodes in the circuit are shared to achieve bidirectional operation. The output capacitors recover secondary-side leakage inductance energy in the step-up mode, and the third winding can be used to recover primary-side leakage inductance energy to reduce the voltage spike on switching in order to improve the converter's conversion efficiency. A 500-W three-port bidirectional converter is implemented to verify the feasibility and practicability of the proposed topology. According to the measurement results, the highest efficiency of the PV step-up mode is 95.3%, the highest efficiency of the battery step-up mode is 94.1%, and the highest efficiency of the step-down mode is 94.8%.

Keywords: three-port bidirectional converter; three-winding coupled inductor

1. Introduction

Climate change and the greenhouse effect are becoming an increasingly major threat to human life and the environment worldwide. Although fossil fuels are exhaustible and contribute greatly to greenhouse emissions, oil remains a primary energy source. With the increasing need to reduce greenhouse emissions and continued growth of energy demand, energy development will face even more severe challenges. At this critical moment in the global energy transition, renewable green energy development will play a key role in leading the third industrial revolution by replacing fossil-fuel-based energy to reduce environmental pollution and promote economic development [1].

Green energy is severely affected by environmental factors. For example, solar power generation systems are often affected by the time, intensity, and angle of incident sunshine; these factors affect the stability of power supply and, in turn, power generation. Therefore, although green energy is a relatively clean energy source, it is inconvenient and unstable to use.

Three-port bidirectional converters are appealing alternatives. Figure 1 illustrates the general application diagram of a three-port bidirectional converter. Taking the solar power generation system as the starting point, we consider how to make the best use of the green energy produced. Solar power systems use solar energy for energy production, therefore the lack of sunshine would lead to inadequate energy. Therefore, an energy storage system must be developed to store more energy during the day

or to satisfy excess energy demands through a battery. When a solar system generates insufficient or no energy owing to environmental factors or at night, energy will be supplied by a battery, thereby considerably improving the stability of the energy system [2–6].

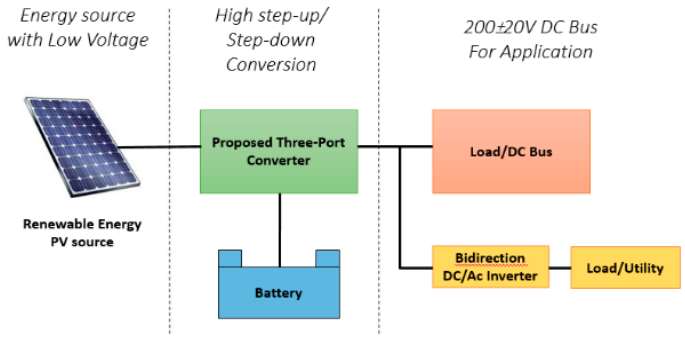

Figure 1. Application diagram of three-port bidirectional converter.

In general, the output voltage of a green energy source must be converted by a dc/dc converter for applying to a dc bus or dc loads. A conventional isolated converter [7–9], such as a flyback converter, forward converter, and push-pull converter, is widely used for this purpose because it improves safety and noise immunity, provides galvanic isolation, and enables adding more windings on the transformer to output multiple voltage values. In recent years, switches shared in the circuit have reached the same topology as the step-up/step-down function of bidirectional converters [9–14]. A common nonisolated bidirectional converter such as a buck/boost bidirectional converter has also been widely used [15]; such a converter has the advantages of a relatively low component count and cost but the disadvantage of a poor voltage conversion ratio. In high-efficiency bidirectional conversion executed using a coupled inductor converter [16] and a bidirectional Sepic-Zeta converter [17], a clamp capacitor can be applied to reduce the voltage stress and recover stray energy; however, such converters do not have an electrical isolation function, making the circuit and switch control signals susceptible to interference. In addition, many isolated bidirectional converters have been proposed recently. For example [18–20] proposed a high-efficiency single-input multiple-output bidirectional isolated converter in which the leakage inductance energy of the coupled inductor is recovered through the clamp capacitor to the power supply terminal and zero-voltage switching (ZVS) is implemented in the converter switch to reduce the switching loss; however, the auxiliary power supply terminal cannot be stepped down/stepped up to other power supply terminals in this topology. Another study [21] proposed a high-conversion-ratio isolated bidirectional converter with a half-bridge LLC topology and dc-blocking capacitor on the high-voltage side. This converter reduces the voltage on the transformer and uses a current multiplying circuit on the low-voltage side to reduce the output ripple current; however, its component count is large and the magnetizing inductance has an energy release problem in high-power applications.

Therefore, this study proposes a three-port bidirectional converter with three-winding coupled inductors. To satisfy the demands of green energy applications, the converter has three operating stages. When the energy supplied from the photovoltaic (PV) modules is sufficient, the converter operates in Stage 1. The PV modules provide energy to the dc bus and simultaneously charge the battery. However, when the energy supplied by the PV modules is insufficient, the converter operates in Stage 2. The battery steps up energy to the dc bus. When the energy supplied from the PV modules cannot charge the battery, the converter operates in Stage 3; the dc bus steps down to the battery.

2. Proposed Converter and Operating Principles

This study proposes a three-port bidirectional converter with three-winding coupled inductors (Figure 2). A three-winding common core coupled inductor is designed and adopted in the proposed converter, and full-wave voltage doubler rectification is used on the high-voltage side to achieve a high step-up effect. The power switches and diodes in the circuit are shared to achieve bidirectional

operation. The output capacitor can recover the secondary-side leakage inductance energy in the step-up mode, and the third winding can be used to recover the primary-side leakage inductance energy to reduce the surge voltage on the switch; thus, the converter can achieve improved conversion efficiency and the charging inductance of the battery side can modify the output voltage value to the battery and protect the battery from the inrush current, thereby extending the battery's lifetime.

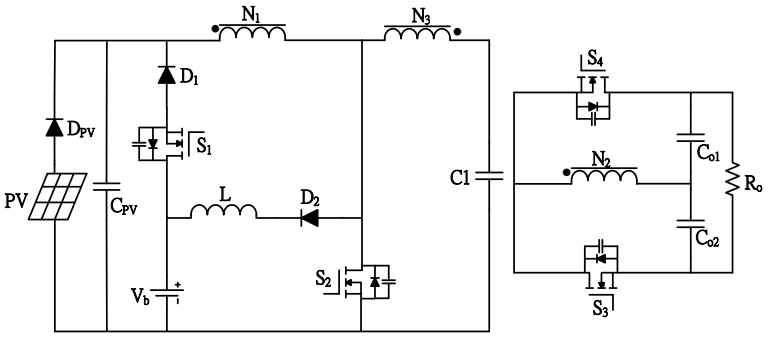

Figure 2. Novel three-port bidirectional converter with three-winding coupled inductors.

This converter has three operating stages. In Stage 1, when the energy supplied from the PV modules is sufficient, the PV module is stepped up to the dc bus and charges the battery, and when the battery is fully charged, the energy is independently supplied to the dc bus. In Stage 2, when the energy supplied from the PV modules is insufficient, the battery is independently stepped up to the dc bus. In Stage 3, when no solar energy is incident or the battery needs to be charged, the dc bus is stepped down to charge the battery. To simplify the circuit analysis, the following conditions are assumed:

(1) Switches S_{1-4} and diodes D_{1-2} are ideal components.
(2) Capacitances C_{PV}, Co_1, and Co_2 are sufficiently large to be considered a constant voltage source.
(3) Each magnetizing inductance of the transformer is much larger than its leakage inductance.

A. Stage 1: PV Output Voltage is stepped up to DC Bus and Charges the Battery

When the energy supplied from the PV modules is sufficient, the PV module voltage is stepped up to the dc bus and charges the battery. Figure 3 illustrates the waveform diagram of main component operation in Stage 1.

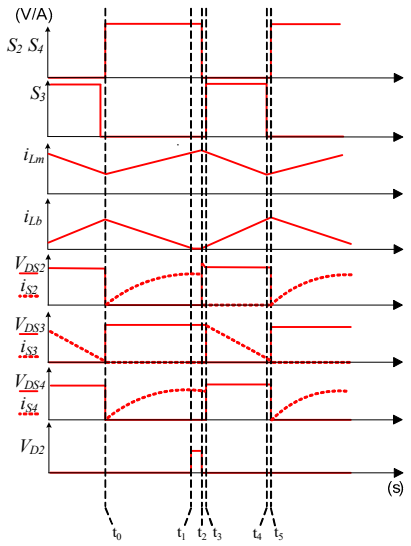

Figure 3. Stage 1 waveform diagram of the main component operation.

(1) Mode I (t_0-t_1):

As displayed in Figure 4a, in this mode, switches S_2 and S_4 are turned on, the other switches are turned off, and the diode D_2 is turned on. The switch S_4 performs synchronous rectification, and the PV module voltage V_{PV} stores energy in the magnetizing inductance L_m and charges the capacitor $C1$ through the third winding; energy is transmitted to the secondary side in the forward direction and charges the capacitor Co_1 through the switch S_4. The output capacitors Co_1 and Co_2 supply energy to the load Ro. The charging inductor L releases energy to the battery. When the current of the charging inductor i_L is equal to zero, this mode ends.

(2) Mode II (t_1-t_2):

As presented in Figure 4b, in this mode, the switches S_2 and S_4 are turned on, the other switches are turned off, and the diode D_2 is turned off. The circuit operates in the same manner as in Mode I. The PV module voltage V_{PV} continuously stores energy in the magnetizing inductance L_m, charges the capacitor C_1 through the third winding, and simultaneously transmits the energy to the secondary side and charges the capacitor Co_1 through the switch S_4. The output capacitors Co_1 and Co_2 supply energy to the load Ro.

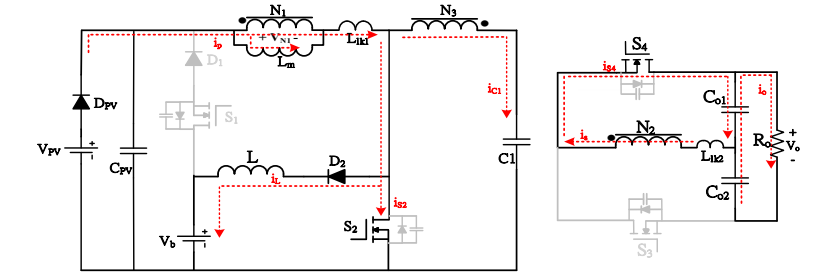

(**a**) Mode I.

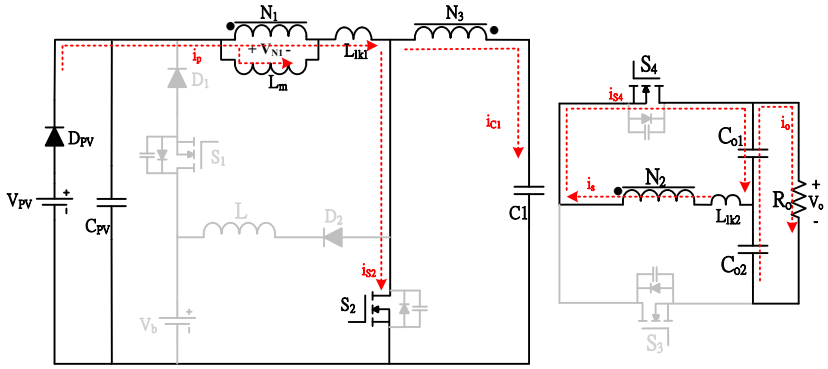

(**b**) Mode II.

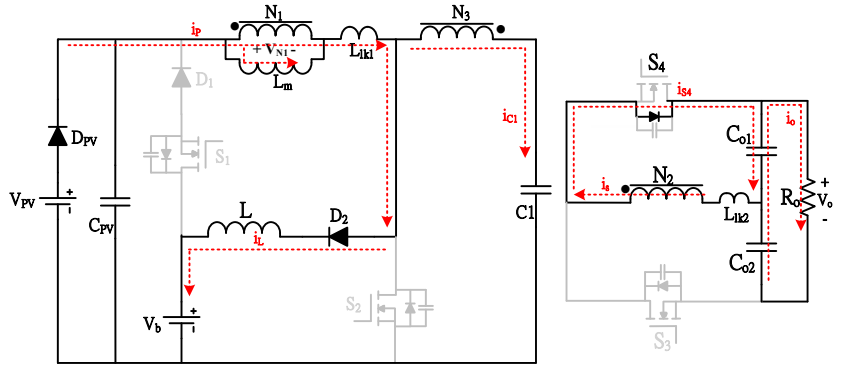

(**c**) Mode III.

Figure 4. *Cont.*

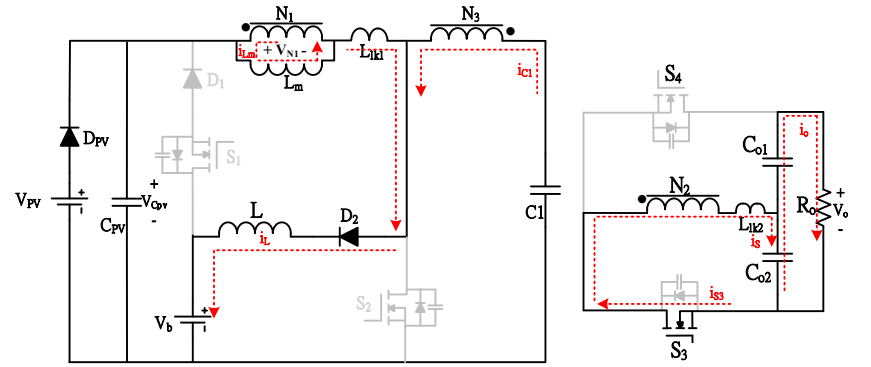

(**d**) Mode IV.

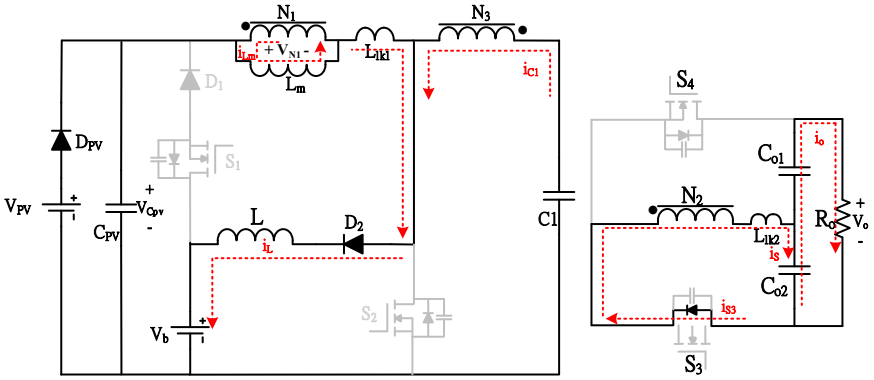

(**e**) Mode V.

Figure 4. Operational diagram of each mode in Stage 1: (**a**) Mode I, (**b**) Mode II, (**c**) Mode III, (**d**) Mode IV, and (**e**) Mode V.

(3) Mode III (t_2-t_3):

As shown in Figure 4c, in this mode, the parasitic diode of the switch S_4 is turned on, the other switches are turned off, and the diode D_2 is turned on. The switch S_4 ends the synchronous rectification, and the primary-side leakage inductance releases energy to inductor L and charges the capacitor C_1 through the third winding. The secondary-side leakage inductance L_{lk2} continues to flow and charges the capacitor Co_1 with the secondary-side energy through the parasitic diode of the switch S_4. The energy is supplied to the load Ro at the same time as Co_1 and Co_2.

(4) Mode IV (t_3-t_4):

As illustrated in Figure 4d, in this mode, the switch S_3 is turned on for synchronous rectification, the other switches are turned off, and the diode D_2 is turned on. The magnetizing inductance L_m can be reversely transmitted to the secondary side through the transformer and charges the capacitor C_{o2} through the switch S_3. The capacitor C_1 is discharged through the third winding. Part of the energy of the magnetizing inductance and the capacitor C_1 is released to the battery and the charging inductor L. The output capacitors C_{o1} and C_{o2} provide energy to the load R_o.

(5) Mode V (t_4-t_5):

As displayed in Figure 4e, in this mode, the parasitic diode of the switch S_3 is turned on, the other switches are turned off, and the diode D_2 is turned on. The switch S_3 ends synchronous rectification, and the rest of the circuit operates in the same manner as in Mode IV. Magnetizing inductance L_m continuously releases energy to the secondary side through the transformer and charges the capacitor Co_2 through the parasitic diode of the switch S_3. Part of the energy of the magnetizing inductance is stored in the charging inductor L and charges the battery. The secondary-side leakage inductance L_{lk2}

freewheels and charges the capacitor Co_2. The output capacitors Co_1 and Co_2 provide energy to the load Ro.

B. Stage 2: Battery Provides Energy to DC Bus

When the energy supplied from the PV modules is insufficient, the battery is independently stepped up to the dc bus. Figure 5 presents the waveform diagram for the operation of the main components in Stage 2.

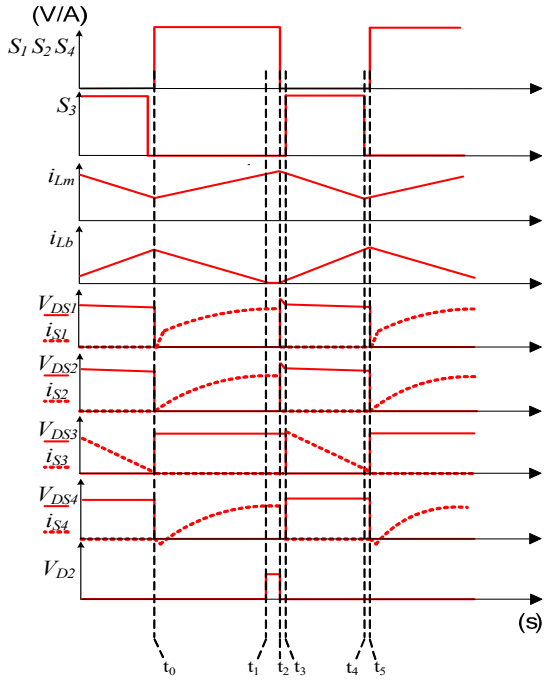

Figure 5. Waveform diagram of operation of main components in Stage 2.

(1) Mode I (t_0-t_1):

As shown in Figure 6a, in this mode, the switches S_1, S_2, and S_4 are turned on; the other switches are turned off; and the diodes D_1 and D_2 are turned on. The battery voltage V_b stores energy in the magnetizing inductance L_m and charges the capacitors C_{PV} and C_1. The output capacitors C_{o1} and C_{o2} supply energy to the load R_o. The charging inductor L releases energy to the battery. When the current of the charging inductor i_L is equal to zero, this mode ends.

(2) Mode II (t_1-t_2):

As illustrated in Figure 6b, in this mode, the switches S_1, S_2, and S_4 are turned on; the other switches are turned off; the diode D_1 is turned on; and the diode D_2 is turned off. The circuit operates in the same manner as in Mode I. The battery input voltage V_b continuously stores energy in the magnetizing inductance L_m and charges the capacitor C_1 through the third winding. Concurrently, energy is induced to the secondary side and charges the capacitor C_{o1} through the switch S_4. The output capacitors C_{o1} and C_{o2} supply energy to the load R_o.

(3) Mode III (t_2-t_3):

As displayed in Figure 6c, in this mode, the parasitic diode of the switch S_4 is turned on, the other switches are turned off, the diode D_2 is turned on, and the diode D_1 is turned off. The switch S_4 ends the synchronous rectification. The primary-side leakage inductance L_{lk1} releases energy to the inductor L and charges the capacitor C_1 through the third winding. The secondary-side leakage inductance L_{lk2}

continues to flow and charges the capacitor C_{o1} with the secondary-side energy through the parasitic diode of the switch S_4. The output capacitors C_{o1} and C_{o2} simultaneously supply energy to the load R_o.

(4) Mode IV (t_3-t_4):

As presented in Figure 6d, in this mode, the switch S_3 is turned on for synchronous rectification, the other switches are turned off, and the diode D_2 remains on. The magnetizing inductance L_m induces the secondary side through the transformer in the reverse direction and charges the capacitor C_{o2} through the switch S_3. The capacitor C_1 is discharged through the third winding and stores energy in the battery and the charging inductor L along with part of the energy of the magnetizing inductance. The output capacitors C_{o1} and C_{o2} provide energy to load R_o.

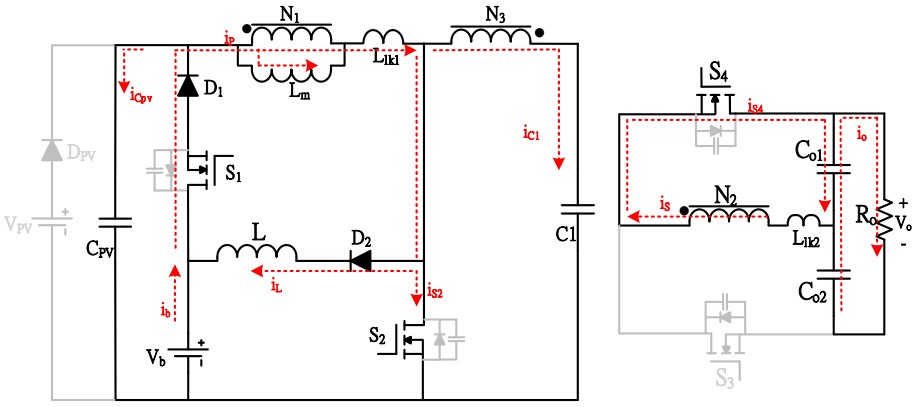

(**a**) Mode I.

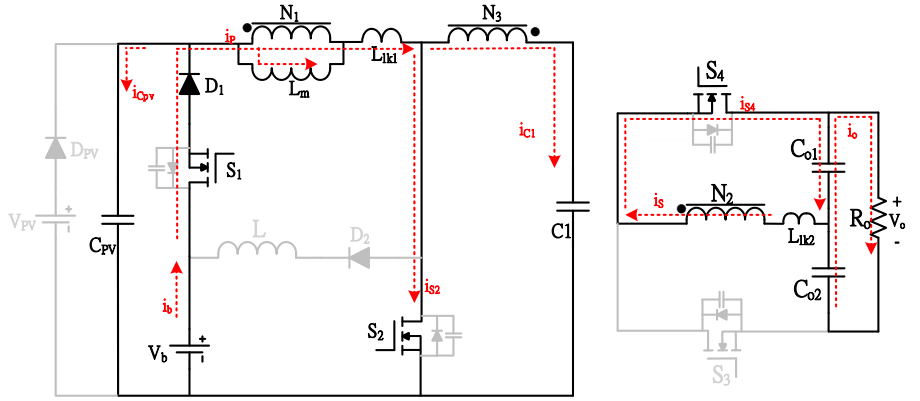

(**b**) Mode II.

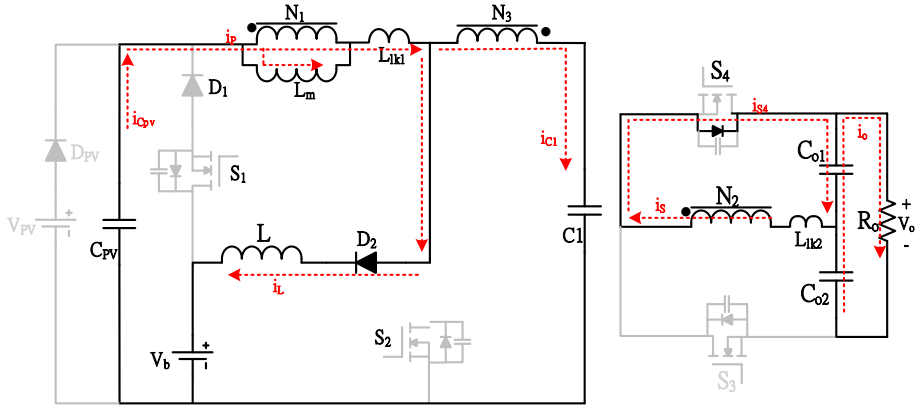

(**c**) Mode III.

Figure 6. *Cont.*

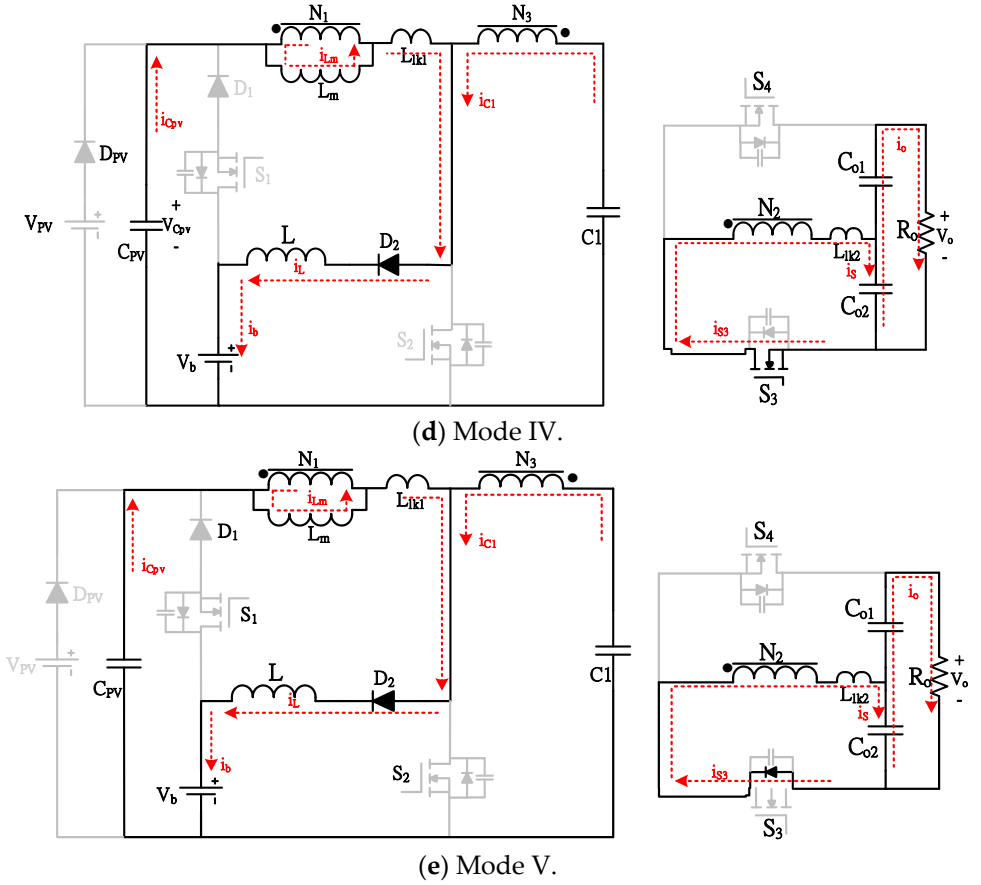

(**d**) Mode IV.

(**e**) Mode V.

Figure 6. Operational diagram of each mode in Stage 2: (**a**) Mode I, (**b**) Mode II, (**c**) Mode III, (**d**) Mode IV, and (**e**) Mode V.

(5) Mode V (t_4-t_5):

As shown in Figure 6e, in this mode, the parasitic diode of the switch S_3 is turned on, the other switches are turned off, and the diode D_2 remains on. The switch S_3 ends the synchronous rectification, and the rest of the circuit operates in the same manner as in Mode IV. The magnetizing inductance L_m continuously releases energy to the secondary side and charges the capacitor C_{o2} through the parasitic diode of switch S_3. Part of the energy of the magnetizing inductance continues to charge the battery and store energy in the charging inductor L. The secondary-side leakage inductance L_{lk2} freewheels and charges the capacitor C_{o2}. The capacitors C_{o1} and C_{o2} supply energy to the load R_o.

C. Stage 3: DC Bus Step Down for Battery Charging

When no solar energy is incident or the battery needs to be charged, the output voltage of the dc bus is stepped down to charge the battery. Figure 7 presents the waveform diagram of the operation of the main components in Stage 3.

(1) Mode I (t_0-t_1):

As shown in Figure 8a, in this mode, the switch S_4 and switch S_2 are turned on for synchronous rectification, the other switches are turned off, and the diode D_2 is turned on. The voltage of the dc bus stores energy in the magnetizing inductance Lm and charges the output capacitor Co_2. The energy induced by the transformer charges the solar input capacitor C_{PV} through the winding N_1 and charges the capacitor C_1 through winding N_3. The charging inductor L is discharged to the battery through the switch S_2.

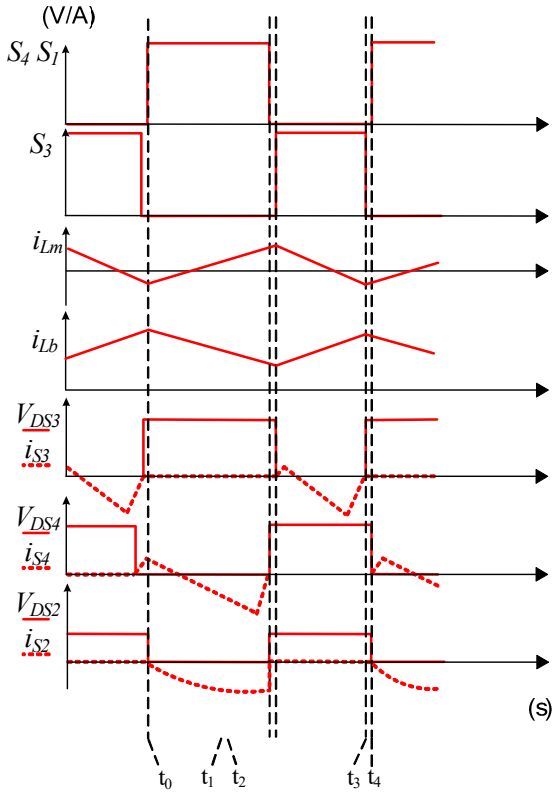

Figure 7. Waveform diagram of operation of main components in Stage 3.

(2) Mode II (t_1-t_2):

As illustrated in Figure 8b, in this mode, the parasitic diode of the switch S_3 is turned on, the other switches are turned off, the diode D_2 is turned on, and the switch S_2 ends the synchronous rectification. The leakage inductance of the transformer L_{lk2} continues to flow and charges the output capacitor C_{o2} through the parasitic diode of the switch S_3. The current induced by the transformer charges the solar input capacitor C_{PV} through the winding N_1 and charges capacitor C_1 through the winding N_3. The charging inductor is continuously discharged to the battery through the parasitic diode of the switch S_2.

(3) Mode III (t_2-t_3):

As displayed in Figure 8c, in this working interval, the switch S_3 is turned on, the other switches are turned off, and the diode D_2 remains on. The magnetizing inductance L_m releases energy to the output capacitor C_{o2} through the switch S_3 and induces the winding N_1 through the transformer. The induced current stores energy in the charging inductor L and charges the battery. The capacitor C_1 is discharged to the battery through the winding N_3.

(4) Mode IV (t_3-t_4):

As presented in Figure 8d, in this mode, the parasitic diode of the switch S_4 is turned on, the other switches are turned off, and the diode D_2 remains on. The leakage inductance of the transformer L_{lk2} charges the output capacitor Co_1 through the parasitic diode of the switch S_4 and induces the winding N_1 through the transformer. The induced current stores energy in the charging inductor and charges the battery. The capacitor C_1 is discharged to the battery through the winding N_3, and the mode ends for one cycle.

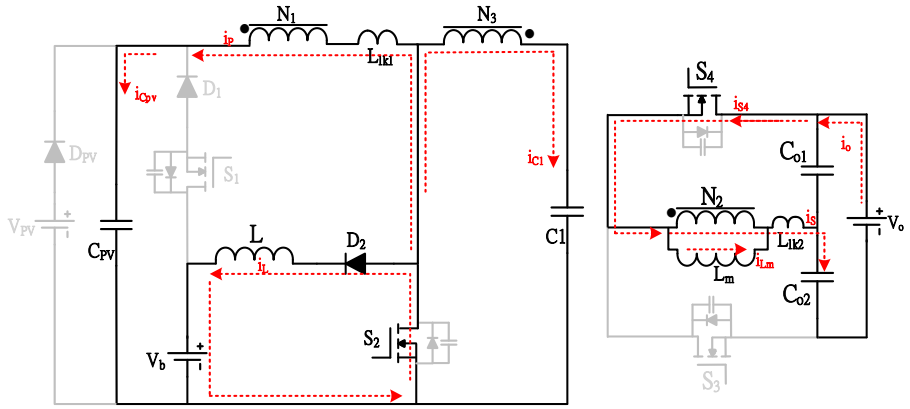

(**a**) Mode I.

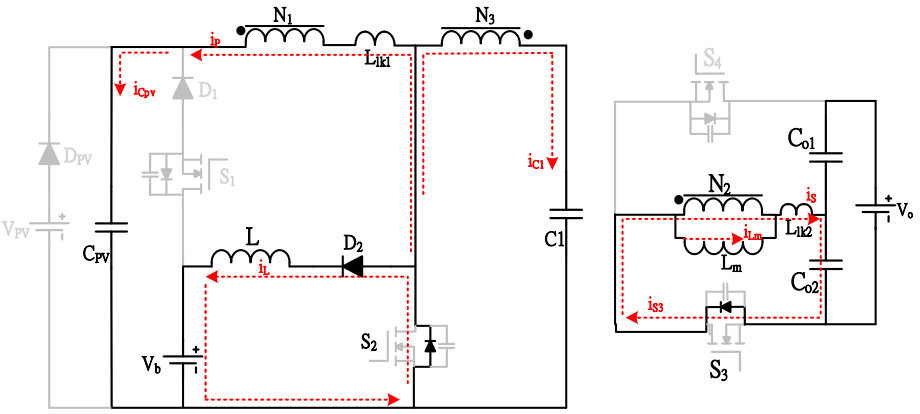

(**b**) Mode II.

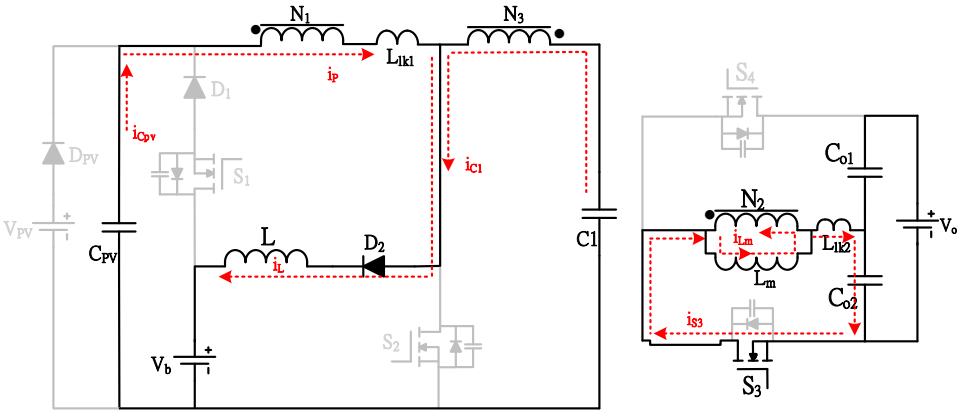

(**c**) Mode III.

Figure 8. *Cont.*

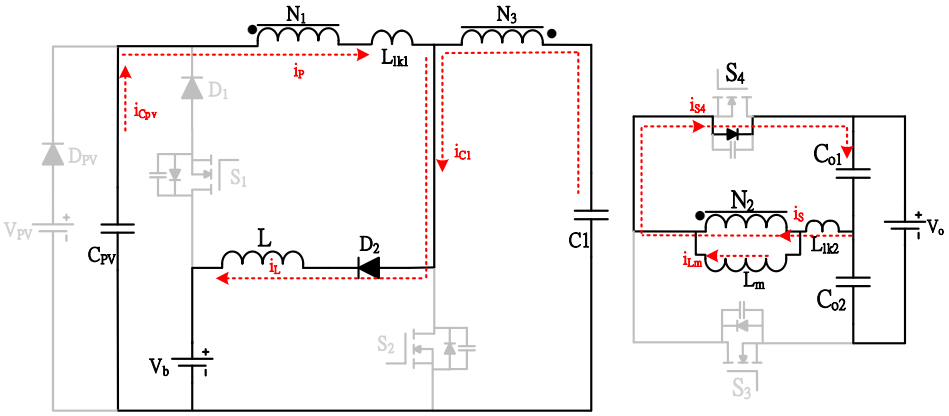

(**d**) Mode IV.

Figure 8. Operational diagram of each mode in Stage 3: (**a**) Mode I, (**b**) Mode II, (**c**) Mode III, and (**d**) Mode IV.

3. Steady-State Analysis

This section focuses on the mathematical derivation of the voltage conversion ratio and voltage stress of components. First, some assumptions are made to simplify the analysis:

(1) All components in the proposed topology are considered ideal components.
(2) The capacitance is sufficiently large to maintain a constant voltage.
(3) Each winding's magnetizing inductance is much larger than its leakage inductance.

A. Voltage Conversion Ratio

Stage 1 is derived such that when solar energy is available, the PV module is stepped up to the dc bus and charges the battery. When the switches S_2 and S_4 are turned on and the other switches are turned off, the voltage on the magnetizing inductance L_m is expressed as

$$V_{L_m} = V_{PV} = V_{o1}\frac{N1}{N2} = L_m\frac{di_L}{dt} \tag{1}$$

The variation of current on the magnetizing inductance L_m is expressed as

$$\Delta {i_{Lm}}^+ = \frac{V_{PV}}{L_m}\,DT \tag{2}$$

When the switch S_3 is turned on and the other switches are turned off, the voltage on the magnetizing inductance L_m is expressed as

$$V_{L_m} = V_{o2}\frac{N1}{N2} = \frac{L_m(di_L)}{dt} \tag{3}$$

The variation of current on the magnetizing inductance L_m is expressed as

$$\Delta {i_{Lm}}^- = \frac{V_{PV} - V_{N1} - V_b}{L}(1-D)T \tag{4}$$

According to the voltage-second balance principle, the variation of current on the magnetizing inductance L_m is constant. Accordingly, the voltage gain of V_o is expressed as

$$\Delta {i_{Lm}}^+ = \Delta {i_{Lm}}^- \tag{5}$$

$$\frac{V_o}{V_{PV}} = \left(\frac{1}{1-D}\right)\frac{N2}{N1} \tag{6}$$

Stage 3 is derived such that when solar energy is unavailable or the battery's power is insufficient, the battery is charged by the dc bus. When the switches S_2 and S_4 are turned on and the other switches are turned off, the voltage on the charging inductor L is expressed as

$$V_L = V_b = L\frac{di_L}{dt} \tag{7}$$

The variation of current on the charging inductor L is expressed as

$$\Delta {i_L}^+ = \frac{V_b}{L}DT \tag{8}$$

When the switch S_3 is turned on and the other switches are turned off, the voltage on the charging inductor L is expressed as

$$V_L = V_{PV} - V_{N1} - V_b = L\frac{di_L}{dt} \tag{9}$$

The variation of current on the charging inductor L is expressed as

$$\Delta {i_L}^- = \frac{V_{PV} - V_{N1} - V_b}{L}(1-D)T \tag{10}$$

In this mode, the voltage V_{N1} on the winding N_1 is expressed as

$$V_{N1} = -V_{L_m}\frac{N1}{N2} \tag{11}$$

According to the voltage–second balance principle, the variation of current on the charging inductor L is constant. Accordingly, the voltage gain of V_b is expressed as

$$\Delta {i_L}^+ = \Delta {i_L}^- \tag{12}$$

$$\frac{V_b}{V_o} = (1-D)\frac{N1}{N2} \tag{13}$$

B. Voltage Stress of Components

The voltage stress of the circuit components can be derived by analyzing their states under on and off operating conditions. The voltage stress of the switch S_2 can be derived from the turned-on state presented in Figure 5a. The switching stress at this time is expressed as

$$V_{PV} = V_{L_m} \tag{14}$$

According to the voltage–second balance principle, the voltage stress of the switch S_2 is expressed as

$$V_{S2} = \frac{V_{PV}}{1-D} \tag{15}$$

When the diode D_1 is assumed to be an ideal component and the switch S_1 is turned off, the voltage stress on the switch is expressed as

$$V_{S1} = V_b - V_{PV} \tag{16}$$

When the switch S_3 is turned off, its voltage stress is obtained from Mode I of Stage 3 illustrated in Figure 8a:

$$V_{S3} = V_o \tag{17}$$

When the switch S_4 is turned off, its voltage stress is obtained from Mode III of Stage 3 presented in Figure 8c:

$$V_{S4} = V_o \tag{18}$$

In Stage 2, the voltage stress of diode D_1 is the same as that of switch S_1.

$$V_{D1} = V_b - V_{PV} \tag{19}$$

When the switch S_2 is turned on, the voltage stress of the diode D_2 is obtained from Mode II of Stage 1 shown in Figure 4b:

$$V_{D2} = V_b \tag{20}$$

The voltage stress of the output capacitors Co_1 and Co_2 is expressed as

$$V_{o1} = V_{o2} = \frac{1}{2}V_o \tag{21}$$

4. Performance Comparison and Experimental Results

To demonstrate the performance and feasibility of the proposed converter and understand the advantages and disadvantages of its architecture, this section presents a comparison of the proposed converter with those in the literature. As presented in Table 1, the proposed converter is separately compared with a bidirectional converter [17,21,22] and a three-port converter [23–25]. The bidirectional converter in [17] uses a clamp capacitor to reduce the voltage stress and recover stray energy, thereby improving the efficiency of the conversion circuit. However, some switches do not perform synchronous rectification, reducing the overall efficiency. The bidirectional converter in [21] is based on a half-bridge LLC topology, and its transformer is considered an ideal transformer; it is used to provide energy to the output load in the forward direction. The dc-blocking capacitor on the high-voltage side reduces the voltage on the transformer, and the current multiplying circuit on the low-voltage side reduces the output ripple current. However, the component count is excessively high, and the output power of this converter is only 200 W. In [22], this topology consists of the voltage doubler circuit, the low-side inductor combined with the transformer to increase power density. The current ripple of this topology is large, therefore the LC filter is added to the voltage ports to reduce the current ripple. This technology not only increases the cost, but also increases the conduction loss.

Table 1. Comparison of the proposed converter with previously reported bidirectional converters.

References	Proposed Paper	Reference [17]	Reference [21]	Reference [22]
Input voltage	24 V	24 V	24 V	40 V
Output voltage	200 V	400 V	200 V	300 V
Output power	500 W	500 W	200 W	400 W
Number of Switch	4	4	4	4
Number of diode	2	0	0	0
Number of Inductor	1	2	2	2
Turn ratio	N = 3	N = 3	N = 1.5	1
Output terminal	2	1	1	1
Operational Mode	3	2	2	2

Table 2 shows a comparison of the proposed converter with other three-port converters [23–25]. The converter in [23] includes an interleaved step-up full-bridge conversion circuit in which switches and diodes are shared to achieve three conversion modes. The converter in [24] uses two inductors to charge the battery in an interleaved manner; the high-voltage side performs full-bridge rectification using switches, and all switches can enable ZVS. However, the number of components such as switches and diodes is excessively high in the converts proposed in [23] and [24], resulting in a significant increase in cost and volume. Owing to output diode blocking, the battery cannot be charged from the output load to achieve bidirectional function. In [25], this topology is composed of two sets of high

step-up converter and a buck converter to achieve the function of a three-port converter. The advantage is that the power can be supplied to the DC bus independently or in parallel. It increases the number of components and the overall volume of the circuit.

Table 2. Comparison of proposed converter with previously reported three-port converters.

References	Proposed Paper	Reference [23]	Reference [24]	Reference [25]
Input voltage	24 V	50 V	42 V	36 V
Output voltage	200 V	370 V	300 V	400 V
Output power	500 W	1 kW	500 W	150 W
Number of Switch	4	4	6	4
Number of diode	2	4	2	5
Number of Inductor	1	3	3	0
Turn ratio	N = 3	N = 4	N = 1.5	N = 4.5
Output terminal	2	2	2	2
Operational Mode	3	3	2	3
Switching frequency	50 kHz	60 kHz	100 kHz	50 kHz

The feasibility of the proposed three-port bidirectional converter with a three-winding coupled inductor is verified through simulations. Next, a 500-W circuit is implemented to verify the study assumptions. Tables 3 and 4 list the electrical and component specifications of the circuit, respectively. Simulated waveforms are evaluated to identify directions for future research. Finally, the voltage and current waveforms of individual components of the implemented circuit are measured to verify its integrity.

Table 3. Electrical specifications of the proposed three-port bidirectional converter.

Parameter	Specification
PV Input Voltage V_{PV}	24~26 V
Battery Voltage V_b	24 V
DC Bus Voltage V_o	200 V
Output Power P_o	500 W
Switching Frequency	50 kHz
Coupling Inductor Turn Ratio	N1: N2: N3 = 1:3:0.4

Table 4. Component specifications.

Component Parameter	Specification
S_1, S_2 (Power MOSFET)	IRFP4321(150 V/78A)
S_3, S_4 (Power MOSFET)	IRFP4868(300 V/70A)
C_{PV} (Electrolytic Capacitor)	100 uF/100 V
C_1 (MPP Film Capacitor)	0.022 uF/100 V
C_{o1} (Electrolytic Capacitor)	82 uF/300 V
C_{o2} (Electrolytic Capacitor)	82 uF/300 V
L (MPP Ring core)	26 uH
magnetizing inductance L_m	10 uH
Diode D_1, D_2	SBR30A45CT(45 V/30A)

In Stage 1, the 24-V PV module supply power is stepped up to a 200-V dc bus and 24-V the battery power, and the waveforms of each component are measured at half load, as illustrated in Figure 9. After the switch is turned off, the switching voltage waveform oscillates because the resonance of the switching parasitic capacitance C_{ds} causes magnetizing and leakage inductances. Figure 9a displays the switch S_2 waveform of the control signal V_{gs2} and switching voltage V_{ds2}, and the voltage stress of S_2 is approximately 80 V. Figure 9b presents the control signal V_{gs2} and the primary-side current waveform of the transformer i_L. Energy storage is performed when the switch S_2 is turned on. Figure 9c shows

the control signal V_{gs2} and the current waveform of the charging inductor i_L. When the switch S_2 is turned off, the charging inductor recovers the magnetizing inductance energy for energy storage. Figure 9d illustrates the switch S_3 waveform of the control signal V_{gs3} and switching voltage V_{ds3}. The voltage stress of S_3 is nearly 200 V of the secondary-side output voltage. Figure 9e shows the switch S_4 waveform of the control signal V_{gs4} and switching voltage V_{ds4}, and the voltage stress of S_4 is approximately 200 V. Figure 9f presents the control signals V_{gs4} and V_{gs3} and the secondary-side current waveform of the transformer i_S. The secondary side stores energy in the output capacitor when the switches S_3 and S_4 are respectively turned on.

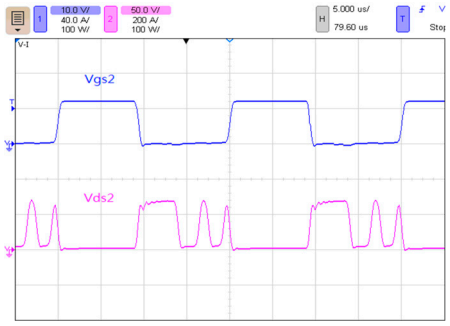

(**a**) (V_{gs2}: 10 V/div,V_{ds2}: 50 V/div)

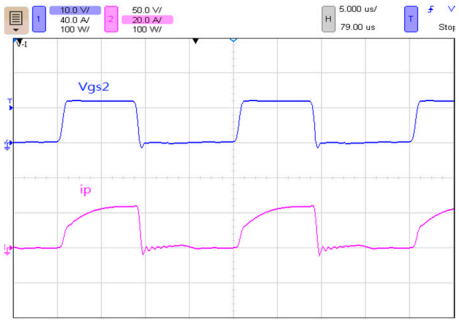

(**b**) (V_{gs2}: 10 V/div, i_P: 20 A/div).

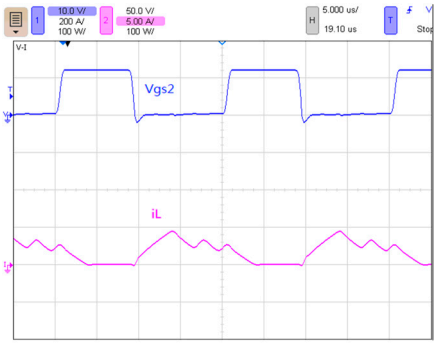

(**c**) (V_{gs2}: 10 V/div, i_L: 5 A/div)

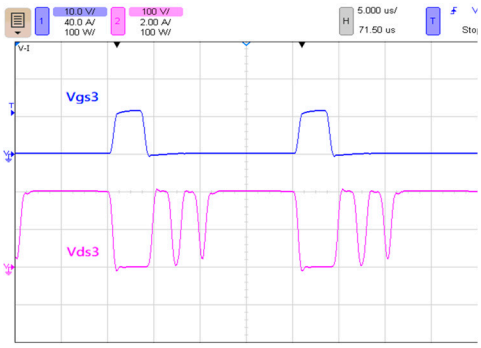

(**d**) (V_{gs3}: 10 V/div, V_{ds3}: 100 V/div).

(**e**) (V_{gs4}: 10 V/div; V_{ds4}: 100 V/div)

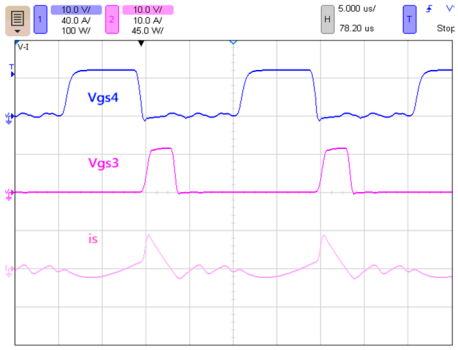

(**f**) (V_{gs4}: 10 V/div, V_{gs3}: 10 V/div, i_s: 10 A/div).

Figure 9. Measured waveforms under Stage 1 at half load: (**a**) switch S_2 waveform, (**b**) primary-side current waveform of transformer, (**c**) charging inductor current waveform, (**d**) switch S_3 waveform, (**e**) switch S_4 waveform, and (**f**) secondary-side current waveform of transformer.

In Stage 1, the waveforms of each component operating at full load are measured (Figure 10). Figure 10a shows the switch S_2 waveform of the control signal V_{gs2} and switching voltage V_{ds2}, and its switching voltage stress is approximately 80 V. Figure 10b illustrates the control signal V_{gs2} and

primary-side current waveform of the transformer i_L. Energy storage is performed when the switch S_2 is turned on. Figure 10c displays the control signal V_{gs2} and current waveform of the charging inductor i_L. When the switch S_2 is turned off, the charging inductor recovers the magnetizing inductance energy for energy storage. Figure 10d presents the switch S_3 waveform of the control signal V_{gs3} and switching voltage V_{ds3}. The switching voltage stress is nearly 200 V. Figure 9e shows the switch S_4 waveform of the control signal V_{gs4} and switching voltage V_{ds4}, and its switching voltage stress is approximately 200 V. Figure 10f illustrates the control signals V_{gs4} and V_{gs3} and secondary-side current waveform of the transformer i_S. The secondary side stores energy in the output capacitor when the switches S_3 and S_4 are respectively turned on.

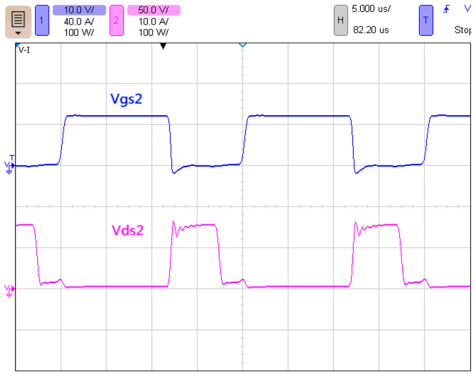

(**a**) (V_{gs2}: 10 V/div,V_{ds2}: 50 V/div)

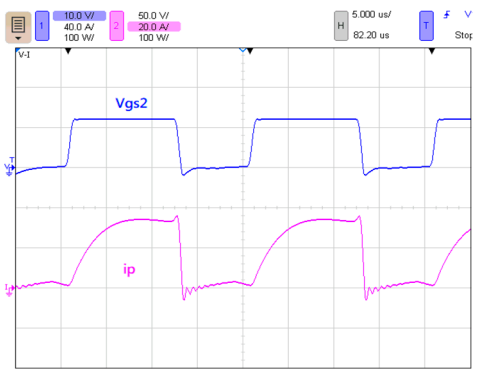

(**b**) (V_{gs2}: 10 V/div, i_P: 20 A/div).

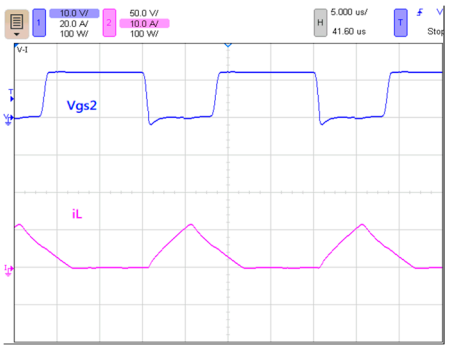

(**c**) (V_{gs2}: 10 V/div, i_L: 5 A/div)

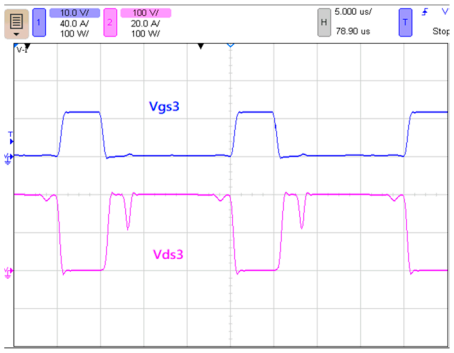

(**d**) (V_{gs3}: 10 V/div, V_{ds3}: 100 V/div).

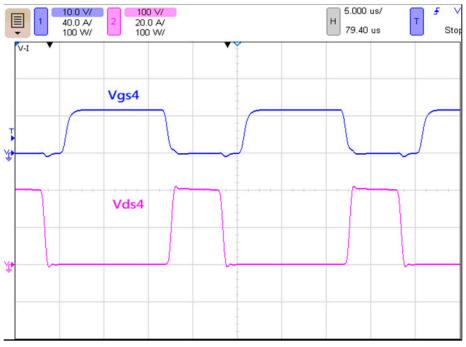

(**e**) (V_{gs4}: 10 V/div; V_{ds4}: 100 V/div)

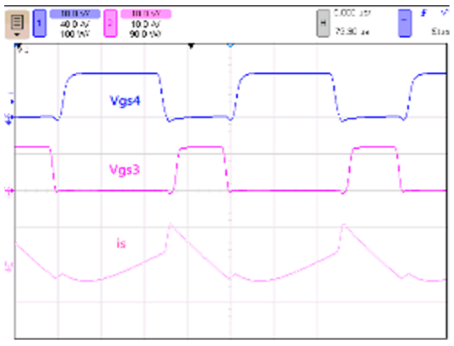

(**f**) (V_{gs4}: 10 V/div, V_{gs3}: 10 V/div, i_s: 10 A/div).

Figure 10. Measured waveforms under Stage 1 at full load: (**a**) switch S_2 waveform, (**b**) primary-side current waveform of transformer, (**c**) charging inductor current waveform, (**d**) switch S_3 waveform, (**e**) switch S_4 waveform, and (**f**) secondary-side current waveform of transformer.

Figure 11 shows the measured waveforms of each component in Stage 2 when the battery of 24 V is stepped up to 200 V corresponding to the dc bus at half load. After the switch is turned off, the switching voltage waveform oscillates the resonance of the switching parasitic capacitance C_{ds} causes magnetizing and leakage inductances. Figure 11a illustrates the switch S_1 waveform of the control signal V_{gs1} and switching voltage V_{ds1}, and its switching voltage stress is approximately 20 V. Figure 11b displays the switch S_2 waveform of the control signal V_{gs2} and switching voltage V_{ds2}, and its switching voltage stress is nearly 80 V. Figure 11c presents the control signal V_{gs2} and primary-side current waveform of the transformer i_L. Energy storage is performed when the switch S_2 is turned on. Figure 11d shows the control signal V_{gs2} and current waveform of the charging inductor i_L. When the switch S_2 is turned off, the charging inductor recovers the magnetizing inductance energy for energy storage. Figure 11e illustrates the switch S_3 waveform of the control signal V_{gs3} and switching voltage V_{ds3}. The switching voltage stress is nearly 200 V. Figure 11f shows the switch S_4 waveform of the control signal V_{gs4} and switching voltage V_{ds4}, and its switching voltage stress is approximately 200 V. Figure 11g presents the control signals V_{gs4} and V_{gs3} and secondary-side current waveform of the transformer i_S. The secondary side stores energy in the output capacitor when the switches S_3 and S_4 are respectively turned on.

In Stage 2, the waveforms of each component operating at full load are measured (Figure 12). Figure 12a shows the switch S_1 waveform of the control signal V_{gs1} and switching voltage V_{ds1}, and its switching voltage stress is approximately 30 V. Figure 12b displays the switch S_2 waveform of the control signal V_{gs2} and switching voltage V_{ds2}, and its switching voltage stress is nearly 80 V. Figure 12c illustrates the control signal V_{gs2} and primary-side current waveform of the transformer i_L. Energy storage is performed when the switch S_2 is turned on. Figure 12d presents the control signal V_{gs2} and current waveform of the charging inductor i_L. When the switch S_2 is turned off, the charging inductor recovers the magnetizing inductance energy for energy storage. Figure 12e shows the switch S_3 waveform of the control signal V_{gs3} and switching voltage V_{ds3}. The switching voltage stress is approximately 200 V. Figure 12f shows the switch S_4 waveform of the control signal V_{gs4} and switching voltage V_{ds4}, and its switching voltage stress is nearly 200 V. Figure 12g displays the control signals V_{gs4} and V_{gs3} and secondary-side current waveform of the transformer i_S. The secondary side stores energy in the output capacitor when the switches S_3 and S_4 are respectively turned on.

Figure 13 presents the measured waveforms of each component in Stage 3 when the 200-V dc bus power is stepped down to the 24-V battery power at half load. This mode of operation is equivalent to the reverse circuit, and the switches S_3 and S_4 are used as complementary control signals. Figure 13a displays the switch S_3 waveform of the control signal V_{gs3} and switching voltage V_{ds3}, and the switching voltage stress is approximately 200 V. Figure 13b illustrates the switch S_4 waveform of the control signal V_{gs4} and switching voltage V_{ds4}, and the switching voltage stress is nearly 200 V. Figure 13c shows the current waveforms of the transformers i_P and i_S. Figure 13d shows the switch S_2 waveform of the control signal V_{gs2}, switching voltage V_{ds2}, and inductor current waveform i_L. The switches S_2 and S_4 are synchronously rectified, and the switching voltage stress is approximately 70 V. The charging inductor is discharged when the switch S_2 is turned on.

Figure 14 illustrates the measured waveforms of each component in Stage 3 at full load. Figure 14a shows the switch S_3 waveform of the control signal V_{gs3} and switching voltage V_{ds3}, and the switching voltage stress is approximately 200 V. Figure 14b shows the switch S_4 waveform of the control signal V_{gs4} and switching voltage V_{ds4}, and the switching voltage stress is nearly 200 V. Figure 14c presents the current waveform of the transformers i_P and i_S. Figure 14d shows the switch S_2 waveform of the control signal V_{gs2}, switching voltage V_{ds2}, and inductor current waveform i_L. The switches S_2 and S_4 are synchronously rectified, and the switching voltage stress is approximately 80 V. The charging inductor is discharged when the switch S_2 is turned on.

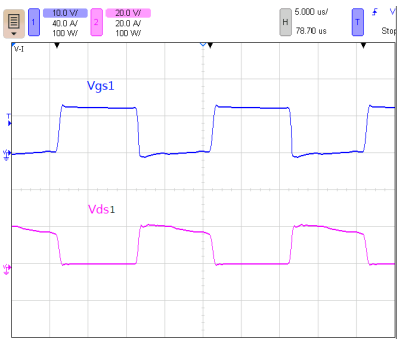

(**a**) (V_{gs1}: 10 V/div,V_{ds1}: 20 V/div)

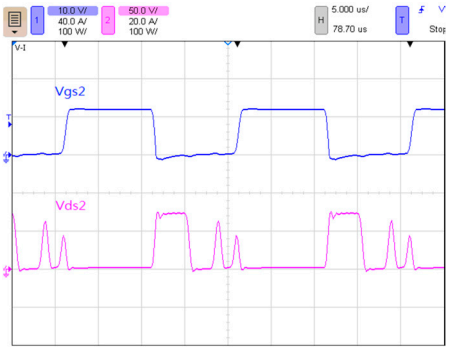

(**b**) (V_{gs2}: 10 V/div, V_{ds2}: 50 V/div).

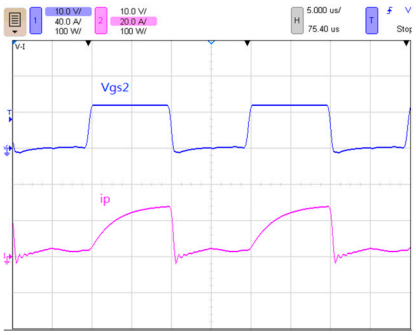

(**c**) (V_{gs2}: 10 V/div, i_p: 20 A/div)

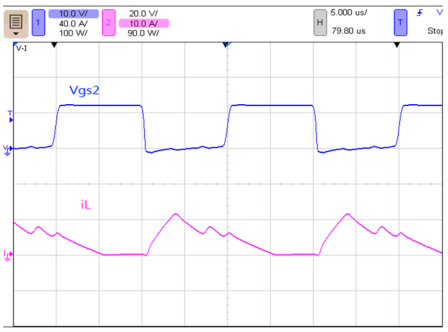

(**d**) (V_{gs2}: 10 V/div, i_L: 10 A/div).

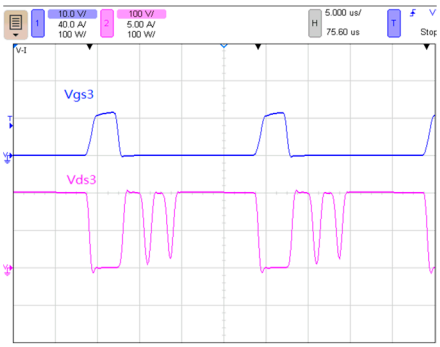

(**e**) (V_{gs3}: 10 V/div; V_{ds3}: 100 V/div)

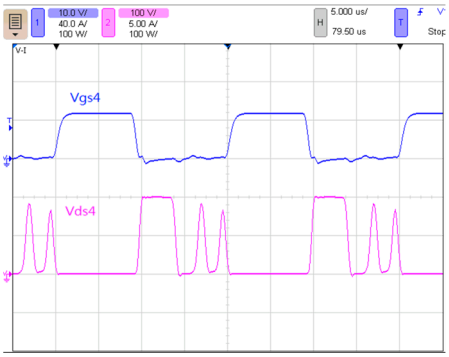

(**f**) (V_{gs4}: 10 V/div, V_{ds4}: 100 V/div).

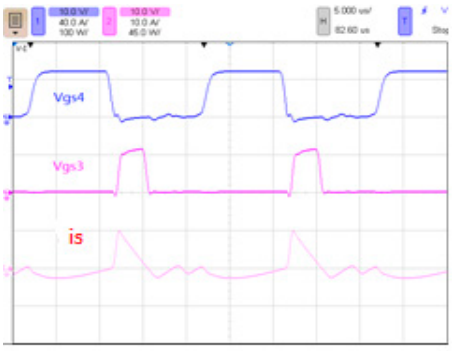

(**g**) (V_{gs4}: 10 V/div, V_{gs3}: 10 V/div, i_s: 10 A/div).

Figure 11. Measured waveforms under Stage 2 at half load: (**a**) switch S_1 waveform, (**b**) switch S_2 waveform, (**c**) primary-side current waveform of transformer, (**d**) charging inductor current waveform, (**e**) switch S_3 waveform, (**f**) switch S_4 waveform, and (**g**) secondary-side current waveform of transformer.

Figure 15 illustrates efficiency diagrams of the three modes of the proposed three-port bidirectional converter. In Stage 1, when the output power is 200 W, the highest efficiency is 95.3%; when the output power is 500 W, the efficiency is 91.3%. In Stage 2, when the output power is 250 W, the highest efficiency is 94.1%; when the output power is 500 W, the efficiency is 90.9%. In Stage 3, when the output power is 250 W, the highest efficiency is 94.8%; when the output power is 500 W, the efficiency is 91.8%.

Figure 16 shows a comparison of the measured PV step-up efficiency of the proposed converter with those of the converters proposed in [17,21,22]. This figure indicates that the efficiency of the proposed converter is higher than that of the converter in [17] but lower than that of the converter in [21] and [22] under light load. However, the converter proposed in [21] has only two modes, whereas the proposed topology herein has three modes and a relatively large output power. Although the converter proposed in [22] has higher efficiency at light load, the efficiency decreases rapidly at more than half load, which is worse than the proposed topology.

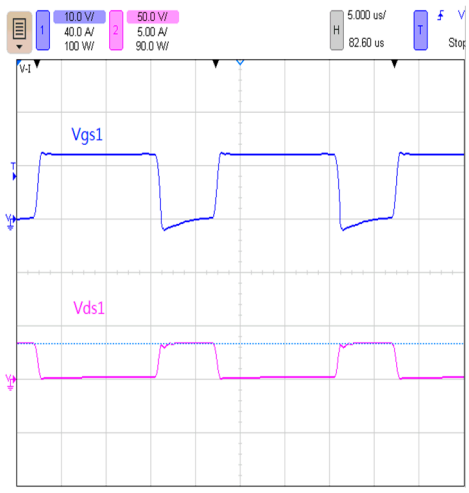

(**a**) (V_{gs1}: 10 V/div,V_{ds1}: 50 V/div)

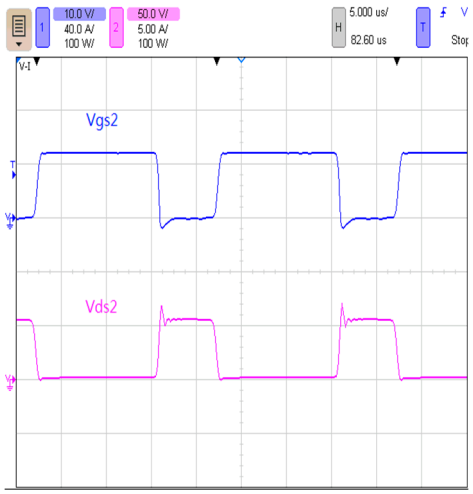

(**b**) (V_{gs2}: 10 V/div, V_{ds2}: 50 V/div).

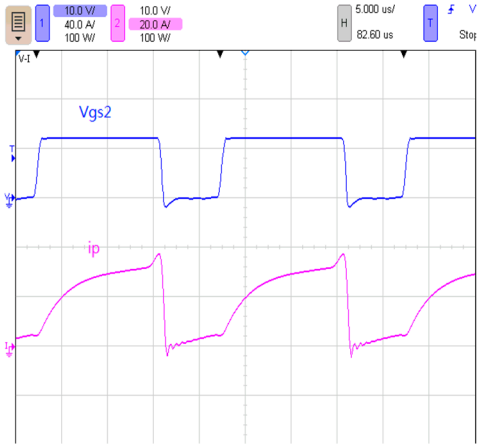

(**c**) (V_{gs2}: 10 V/div, i_P: 20 A/div)

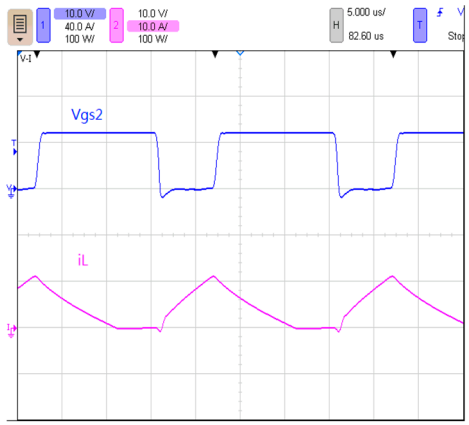

(**d**) (V_{gs2}: 10 V/div, i_L: 10 A/div).

Figure 12. *Cont.*

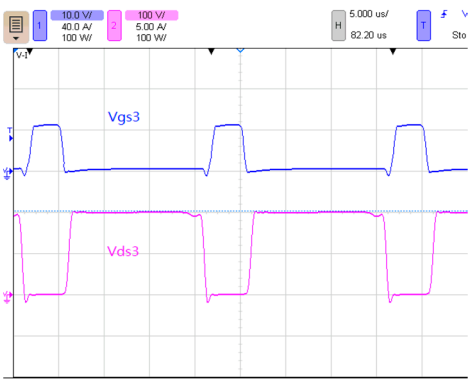

(**e**) (V_{gs3}: 10 V/div; V_{ds3}: 100 V/div)

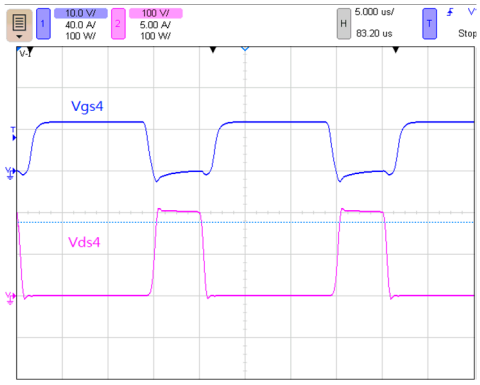

(**f**) (V_{gs4}: 10 V/div, V_{ds4}: 100 V/div).

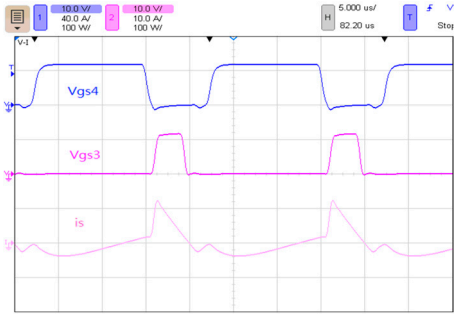

(**g**) (V_{gs4}: 10 V/div, V_{gs3}: 10 V/div, i_s: 10 A/div).

Figure 12. Measured waveforms under Stage 2 at full load: (**a**) switch S_1 waveform, (**b**) switch S_2 waveform, (**c**) primary-side current waveform of transformer, (**d**) charging inductor current waveform, (**e**) switch S_3 waveform, (**f**) switch S_4 waveform, and (**g**) secondary-side current waveform of transformer.

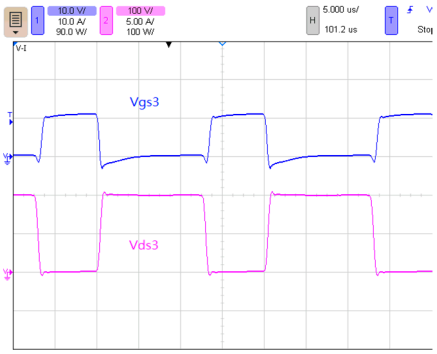

(**a**) (V_{gs3}: 10 V/div,V_{ds3}: 100 V/div)

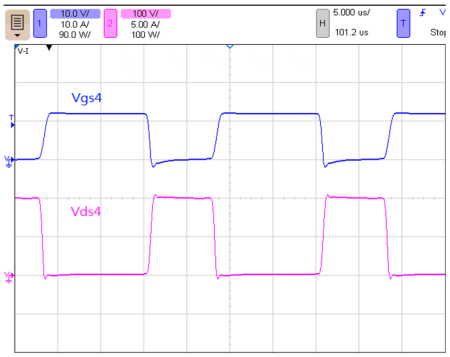

(**b**) (V_{gs4}: 10 V/div, V_{ds4}: 100 V/div).

Figure 13. *Cont.*

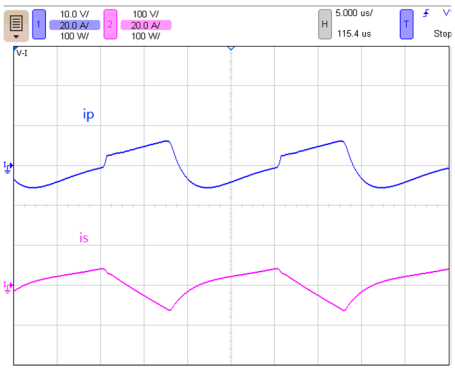

(**c**) (i_p: 20 A/div, i_s: 20 A/div)

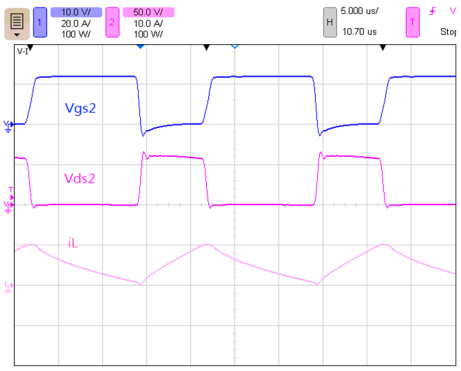

(**d**) (V_{gs2}: 10 V/div, V_{ds2}: 50 V/div,i_L: 10 A/div).

Figure 13. Measured waveforms under Stage 3 at half load: (**a**) switch S_3 waveform, (**b**) switch S_4 waveform, (**c**) current waveform of transformer, and (**d**) switch S_2 waveform and charging inductor current waveform.

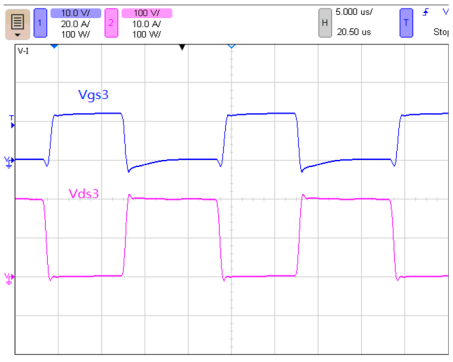

(**a**) (V_{gs3}: 10 V/div, V_{ds3}: 50 V/div)

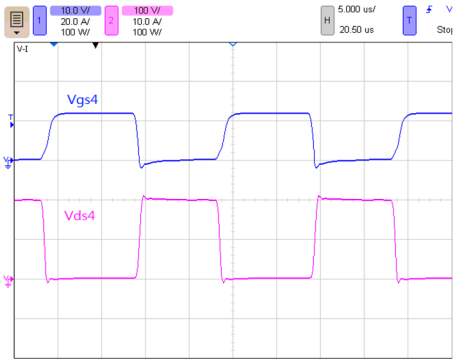

(**b**) (V_{gs4}: 10 V/div, V_{ds4}: 50 V/div).

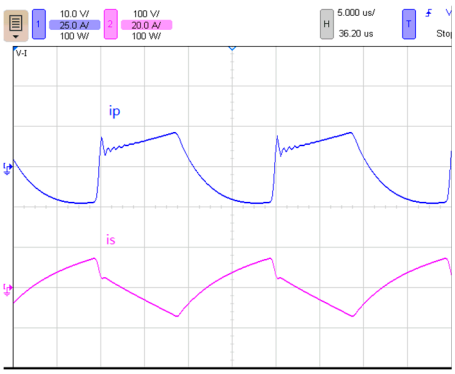

(**c**) (i_p: 25 A/div, i_s: 20 A/div)

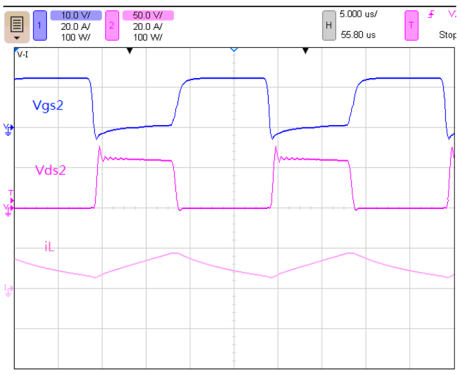

(**d**) (V_{gs2}: 10 V/div, V_{ds2}: 50 V/div, i_L: 20 A/div).

Figure 14. Measured waveforms under Stage 3 of full load: (**a**) switch S_3 waveform, (**b**) switch S_4 waveform, (**c**) current waveform of transformer, and (**d**) switch S_2 waveform and charging inductor current waveform.

Figure 17 shows a comparison of the measured dc bus step-down efficiency of the proposed converter what those of the converters proposed in [17,21,22]. This figure indicates that the efficiency of the proposed converter is higher than that of the converter in [17] but lower than that of the converter in [21]. However, the converter proposed in [21] has only two modes and a lower output power than does the proposed converter. Although the converter proposed in 24 has higher efficiency, its step-down ratio is only twice, which is lower than the proposed topology.

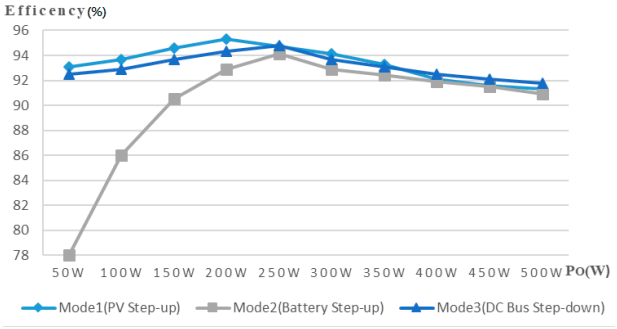

Figure 15. Efficiency curve of proposed three-port bidirectional converter.

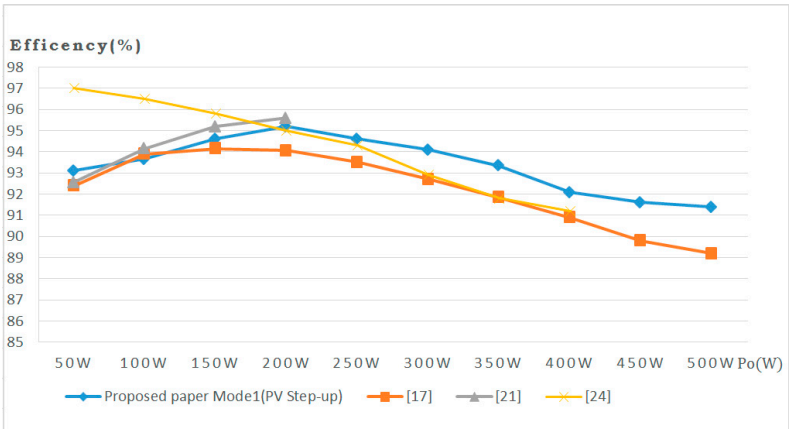

Figure 16. Efficiency comparison of proposed method and methods proposed in Refs. [17,21,22] in step-up mode.

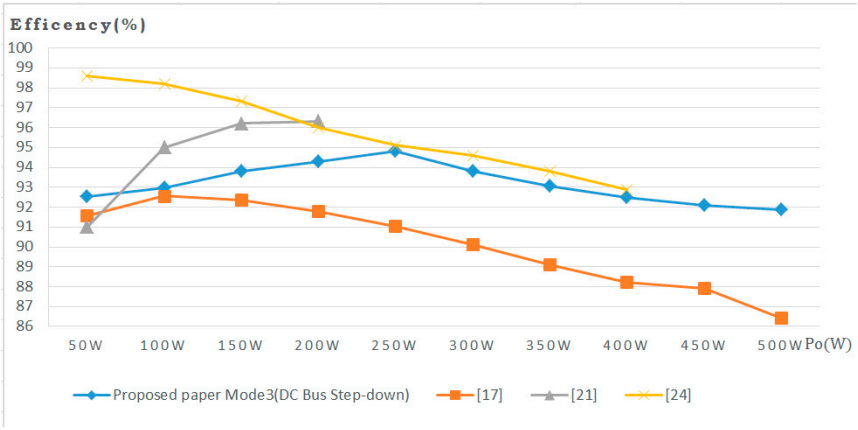

Figure 17. Comparison of efficiency of proposed converter with those of converters proposed in [17,21,22] in step-down mode.

In Figure 18, the measured efficiency of PV step up to dc bus stage observed for the proposed converter is compared with those observed for the converters proposed in [23–25]. This figure indicates that the light and half load efficiency is higher than those obtained in [23] and [24] and that the number of components is lower; therefore, the cost is low. The converter proposed in [25] consists of two sets of independent high step-up converter, the conversion efficiency is higher, but its power implemented is only 150 W and cost is also relatively higher.

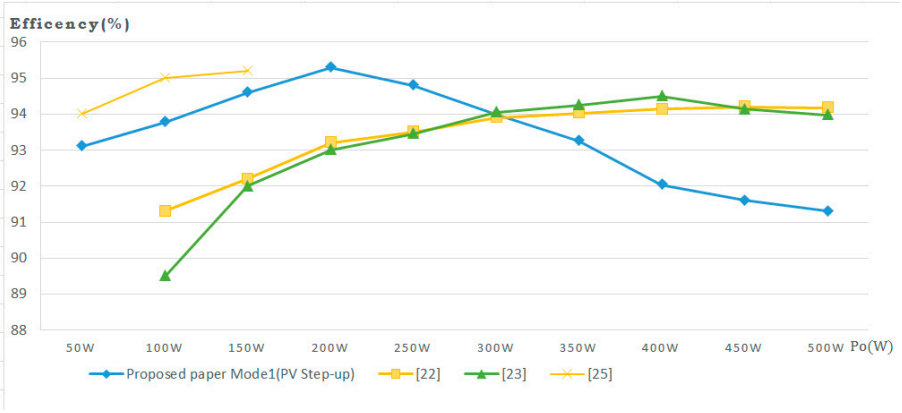

Figure 18. Comparison of efficiency of proposed converter with those of converters proposed in [23–25] in step-up mode.

Figure 19 depicts the printed circuit board layout of the proposed three-port bidirectional converter.

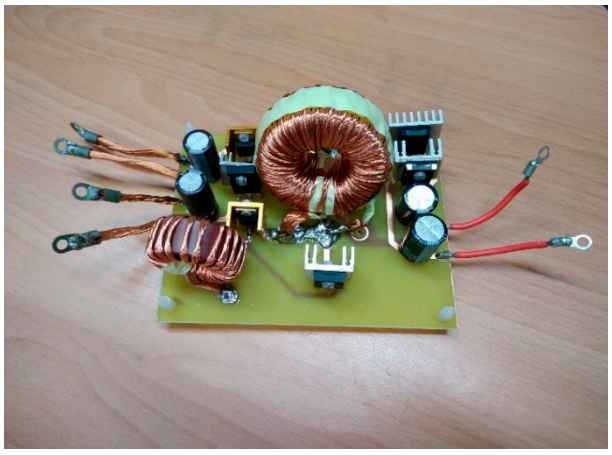

Figure 19. Photograph of proposed three-port bidirectional converter.

5. Conclusions

This study proposes a three-port bidirectional converter with a three-winding common core coupled inductor and a full-wave doubler circuit on the high-voltage side to achieve high step up. Power switches and diodes in the circuit are shared to achieve bidirectional operation. The effectiveness and feasibility of the proposed architecture are verified through action mode analysis, steady-state analysis, and circuit design methods as well as through a simulation and implementation. Finally, according to the study results, a circuit with a full load output of 500 W is implemented. The highest efficiency of the PV module step-up mode is 95.3%, the highest efficiency of the battery step-up mode is 94.1%, and the highest efficiency of the dc bus step-down mode is 94.8%.

Author Contributions: DC/DC Converter Topology, Y.-E.W.; Hardware implementation, K.-C.H. All authors have read and agreed to the published version of the manuscript.

Funding: This research received no external funding.

Conflicts of Interest: The authors declare no conflict of interest.

References

1. Ministry of Economic Affairs, Energy Bureau, Global Information Network. Available online: https://www.moeaboe.gov.tw/ECW/populace/home/Home.aspx (accessed on 2 April 2017).

2. Ding, S.; Wu, H.; Xing, Y.; Fang, Y.; Ma, X. Topology and control of a family of non-isolated three-port DC-DC converters with a bidirectional cell. In Proceedings of the 2013 Twenty-Eighth Annual IEEE Applied Power Electronics Conference and Exposition (APEC), Long Beach, CA, USA, 17–21 March 2013; pp. 1089–1094.
3. Zhao, J.; Iu, H.H.C.; Fernando, T.; An, L.; Dah-Chuan Lu, D. Design of a non-isolated single-switch three-port DC-DC converter for standalone PV-battery power system. In Proceedings of the 2015 IEEE International Symposium on Circuits and Systems (ISCAS), Lisbon, Portugal, 24–27 May 2015; pp. 2493–2496.
4. Schmitz, L.; Coelho, R.F.; Martins, D.C. High step-up high efficiency dc-dc converter for module-integrated photovoltaic applications. In Proceedings of the 2015 IEEE 13th COBEP/SPEC, Fortaleza, Brazil, 29 November–2 December 2015; pp. 1–6.
5. Cheng, T.; Lu, D.D.C.; Gong, A.; Verstraete, D. Analysis of a three-port DC-DC converter for PV-battery system using DISO boost and SISO buck converters. In Proceedings of the 2015 Australasian Universities Power Engineering Conference (AUPEC), Wollongong, NSW, Australia, 27–30 September 2015; pp. 1–6.
6. Teja, V.R.; Srinivas, S.; Mishra, M.K. A three port high gain non-isolated DC-DC converter for photovoltaic applications. In Proceedings of the 2016 IEEE International Conference on Industrial Technology (ICIT), Taipei, Taiwan, 14–17 March 2016; pp. 251–256.
7. Abraham, I.; Pressman, K.B.; Taylor, M. *Switched Power Supply Design*, 3th ed.; McGraw-Hill Books: New York, NY, USA, 2012.
8. Hart, D.W. *Power Electronics*; Zhonghua Book Company: Beijing, China, 2013.
9. Liang, H.W.R.; Chen, J.; Lim, C. Design and implementation of a bidirectional flyback boost/buck integrated converter. In Proceedings of the 2016 IEEE 2nd Annual Southern Power Electronics Conference, Auckland, New Zealand, 5–8 December 2016; pp. 1–6.
10. Chen, Y.T.; Wei, S.Y. A multiple-winding bidirectional flyback converter used in the solar system. In Proceedings of the 2013 International Symposium on Next-Generation Electronics, Kaohsiung, Taiwan, 25–26 February 2013; pp. 130–133.
11. Song, Y.; Enjeti, P.N. A new soft switching technique for bi-directional power flow, full-bridge DC-DC converter. In Proceedings of the 2002 IEEE Industry Applications Conference, 37th IAS Annual Meeting, Pittsburgh, PA, USA, 13–18 October 2002; pp. 2314–2319.
12. Ma, Z.; Hu, R. Zero-voltage-switching condition of isolated-type symmetrical half-bridge bidirectional DC/DC converter. In Proceedings of the 2011 International Conference on Electrical and Control Engineering, Yichang, China, 16–18 September 2011; pp. 2347–2350.
13. Mohammadi, M.R.; Farzanehfard, H. A new bidirectional ZVS-PWM Cuk converter with active clamp. In Proceedings of the 19th Iranian Conference on Electrical Engineering, Tehran, Iran, 17–19 May 2011; pp. 1–6.
14. Dimna Denny, C.; Shahin, M. Analysis of bidirectional SEPIC/Zeta converter with coupled inductor. In Proceedings of the 2015 International Conference on Technological Advancements in Power and Energy (TAP Energy), Kollam, India, 24–26 June 2015; pp. 103–108.
15. Jianhua, W.; Fanghua, Z.; Chunying, G.; Ran, C. Modeling and analysis of a buck/boost bidirectional converter with developed PWM switch model. In Proceedings of the 8th International Conference on Power Electronics—ECCE Asia, Jeju, Korea, 30 May–3 June 2011; pp. 705–711.
16. Duan, R.-Y.; Lee, J.-D. High-efficiency bidirectional DC-DC converter with coupled inductor. *IET Power Electron.* **2012**, *5*, 115–123. [CrossRef]
17. Lee, H.Y.; Liang, T.J.; Chen, J.F.; Chen, K. Design and implementation of a bidirectional SEPIC-Zeta DC-DC Converter. In Proceedings of the 2014 IEEE International Symposium on Circuits and Systems (ISCAS), Melbourne, VIC, Australia, 1–5 June 2014; pp. 101–110.
18. Wai, R.J.; Liaw, J.J. High-efficiency-isolated single-input multiple-output bidirectional converter. *IEEE Trans. Power Electron.* **2015**, *30*, 4914–4930. [CrossRef]
19. Zhang, B.; Wang, P.; Bei, T.; Li, X.; Che, Y.; Wang, G. Novel topology and control of a non-isolated three port DC-DC converter for PV-battery power system. In Proceedings of the 20th International Conference on Electrical Machines and Systems (ICEMS), Sydney, NSW, Australia, 11–14 August 2017.
20. Chien, L.; Chen, C.C.; Chen, J.F.; Hsieh, Y. Novel three-port converter with high-voltage gain. *IEEE Trans. Power Electron.* **2014**, *29*, 4693–4703. [CrossRef]
21. Liang, T.J.; Lee, J.H. Novel high-conversion-ratio high-efficiency isolated bidirectional DC–DC converter. *IEEE Trans. Ind. Electron.* **2015**, *62*, 4492–4503. [CrossRef]

22. Zhang, Y.; Liu, H.; Li, J.; Sumner, M. A low-current ripple and wide voltage-gain range bidirectional DC–DC converter with coupled inductor. *IEEE Trans. Power Electron.* **2020**, *35*, 1525–1535. [CrossRef]
23. Mira, M.C.; Zhang, Z.; Knott, A. Analysis, design, modeling, and control of an interleaved-boost full-bridge three-port converter for hybrid renewable energy systems. *IEEE Trans. Power Electron.* **2017**, *32*, 1138–1155. [CrossRef]
24. Wu, H.; Zhang, J.; Qin, X.; Mu, T.; Xing, Y. Secondary-side-regulated soft-switching full-bridge three-port converter based on bridgeless boost rectifier and bidirectional converter for multiple energy interface. *IEEE Trans. Power Electron.* **2016**, *31*, 4847–4860. [CrossRef]
25. Faraji, R.; Farzanehfard, H. Soft-switched nonisolated high step-up three-port DC–DC converter for hybrid energy systems. *IEEE Trans. Power Electron.* **2018**, *33*, 10101–10111. [CrossRef]